

Rifts in Rafts

Khá-Î Tô and Sidney R. Nagel

*The Department of Physics and the James Franck and Enrico Fermi Institute
The University of Chicago IL 60637*

(Dated: March 8, 2022)

The failure of materials is often considered as a quasi-static process in classical fracture mechanics. No dynamics can be allowed because the speed of sound is much greater than any other velocity. In this paper, we introduce a macroscopic system where the dynamics of particle relaxation and rift formation can be resolved: a particle aggregate is stretched uniaxially by the expansion of the air-fluid interface on which it floats. The failure morphology of these rafts change continuously with pulling velocity. This can be understood by the competition between two velocities: the speed of particle relaxation towards the nearest low energy configuration (*i.e.*, re-aggregation), which is determined by viscous and capillary forces, and the velocity difference between neighboring particles, which is caused by the expanding underlying fluid. This crossover behavior selects the cluster length scales, *i.e.*, the distance between adjacent rifts, and is consistent with the the experimental failure patterns.

I. INTRODUCTION

The failure of a sheet of material pulled from its two opposing edges is often characterized as being either brittle or ductile [1, 2]. Brittle fracture occurs when a thin crack propagates rapidly across the material breaking it into two pieces [2–4]; ductile failure happens when a large area of the material deforms plastically so that the material is no longer able to withstand the external load [5]. This is an oversimplified dichotomy.

Intermediate situations can be found in quasi-brittle materials in which a region of plastic deformation surrounds the crack while preserving the appearance of brittle fracture at larger scales [6]. In other cases, the shear band used to distinguish a region of deformation inside an otherwise brittle matrix can have a significant width [7, 8]. Simulations have shown that disorder is an important factor in determining the nature of the failure zone [9–12].

In some situations the size of the failure zone can be tuned continuously from the atomic scale (as in an ideally brittle crack) to reach the system size without undergoing significant plastic deformation. In this case, the material rigidity was determined to be the control parameter [13]. As the rigidity of a material sheet is reduced, the width of the failure zone diverges and the speed of propagation decreases by several orders of magnitude. In those experiments and simulations, no rearrangement or bond creation was allowed once a bond was broken. Thus, because there was no rearrangement or change in material shape, it is not possible to describe such failure in terms of material ductility; in that case, the brittle / ductile distinction is inappropriate. We describe this as “distributed failure” because the damage is not confined to a small region of the sample.

In this paper, we investigate the distributed failure of a particle raft composed of sub-millimeter particles floating at an air-liquid surface as it is pulled apart. This is a particularly interesting system because (i) the particles are macroscopic, so that their individual motions can be

resolved, (ii) the pulling speed can be varied over several orders of magnitude, and, most importantly, (iii) the particles can rearrange and find new neighbors as the rifts form and propagate. This allows direct observation of the relaxation. Although this, too, is an example of distributed failure, this system is distinct from the previous example because particle rearrangements occur during the failure process.

Our experiment reveals not only distributed failure but also a complex interaction between the pulling speed and the structural morphology of the failure. As the pulling speed increases, new rifts form throughout the raft as it breaks up into ever-finer structures until, at the highest strain rates, the structures reach the individual particle level. We interpret this behavior as a competition between the pulling speed and the microscopic dynamics of particle relaxation. We have developed a one-dimensional model in which a linear (in)stability analysis provides a good description of this behavior.

Previous studies have examined rafts under tension. In the quasi-static regime, the ductile behavior of particle rafts shows a dependence on particle size at small strains [14]. However, the dependence of the failure morphology on the pulling speed was not examined. In the case of soap-bubble films, a failure pattern as a function of strain rate and system size was investigated but the distributed-failure regime was not accessed [15]. We explore wider dynamical ranges in both strain and strain rate and are able to observe a smooth change in failure morphology of the rafts, including the domain of distributed failure where small rifts formed homogeneously throughout the raft.

A related system is crack formation in a thin material sheet on a *solid* substrate. These include nanoparticle films on expanding polymer membranes [16, 17] and drying colloidal monolayers on glass [18, 19]. In both cases, the systems exhibit cracking patterns throughout the material but with no obvious dependence on the pulling or drying speed. These patterns are governed by the interactions with the underlying solid substrate; the relaxing

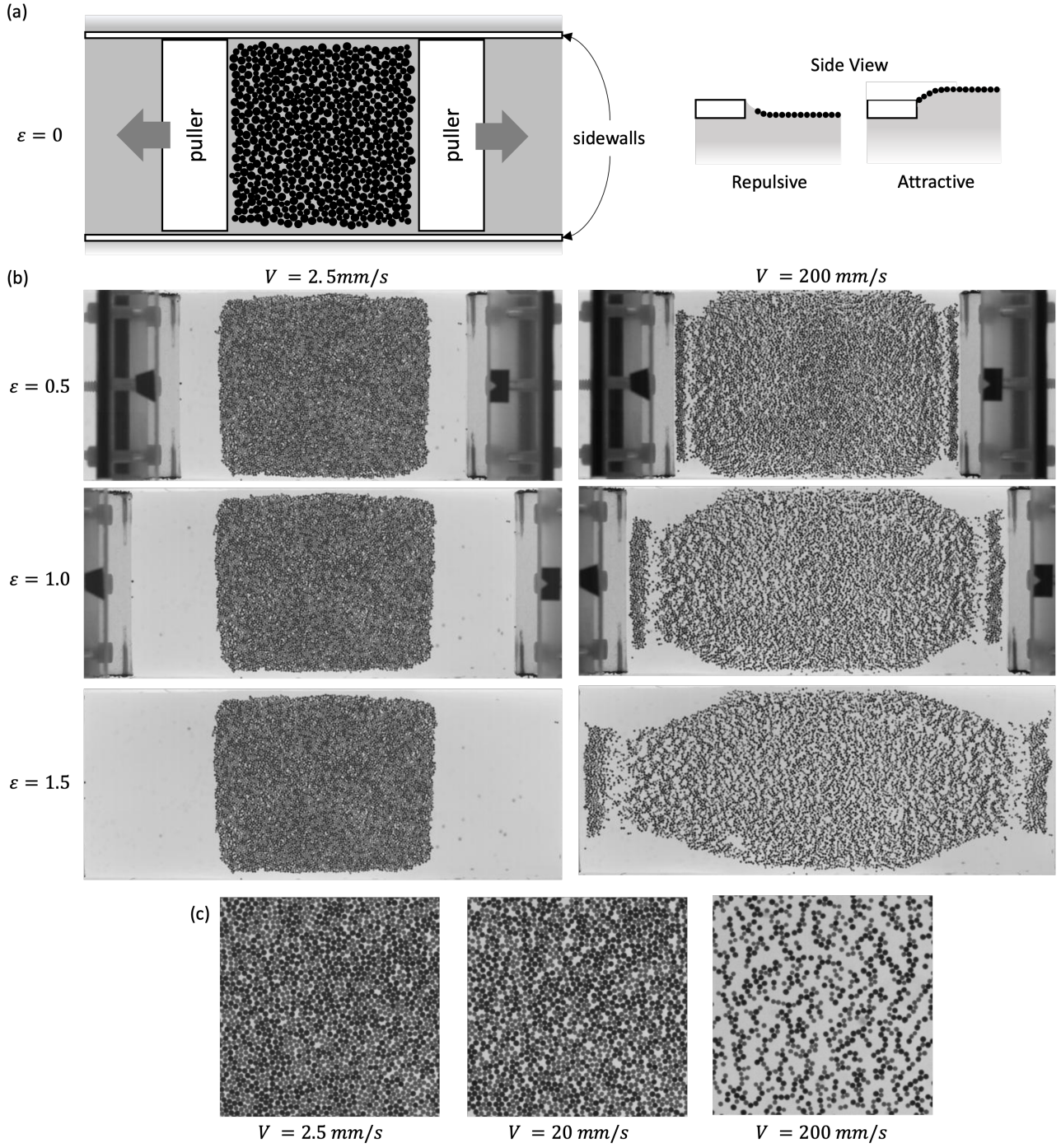


FIG. 1. (a) A schematic of the experimental apparatus. The side view of repulsive and attractive boundaries. (b) Snapshots of air-water experiments at different velocity. Series of images showing the expanding processes at low (2.5 mm/s) and high (200 mm/s) velocities. (c) Zoomed-in images at the bulk of the rafts for $V = 2.5, 20, 200 \text{ mm/s}$.

elastic stress in the thin sheet competes with the interaction holding the sheet to the substrate. In contrast, the system we study is a particle raft on a *liquid* substrate which does not store any shear stress. The mechanism for the formation of distributed failure in these rafts is therefore distinct from what occurs on solid substrates.

The affine expansion of the liquid surface, on which the particles float, can be thought of as a metric for the particle positions which expands in time.

We note that this situation bears a resemblance to cosmic expansion. Our experiment, which measures the cluster formation in the two-dimensional raft as a func-

tion of pulling speed, is similar to the structure formation in three dimensions but on a *much* smaller scale and with overdamped rather than underdamped dynamics.

II. EXPERIMENTAL DETAILS

A schematic of the experimental apparatus is shown in Fig. 1(a). We use rafts comprised of spherical polyethylene particles floating at an air-liquid interface. We use both deionized water (with density $\rho_w = 998 \text{ kgm}^{-3}$; dynamic viscosity $\eta_w = 0.95 \text{ mPas}$ and surface tension, $\sigma_w = 0.073 \text{ Nm}^{-1}$ at 22°C) and a 60 w/w% glycerol-water mixture (with density $\rho_{gw} = 1150 \text{ kgm}^{-3}$, dynamic viscosity $\eta_{gw} = 10.1 \text{ mPas}$, and surface tension $\sigma_{gw} = 0.064 \text{ Nm}^{-1}$ at 22°C) as underlying fluids. Polydisperse packings are made by mixing approximately equal amounts of particles chosen with two diameter ranges: $d = 550 \pm 50 \mu\text{m}$ (small) and $d = 655 \pm 55 \mu\text{m}$ (large). The density of the particles is chosen to be slightly greater than that of the liquid. This creates sufficient lateral capillary attraction (known as the “Cheerios” effect [20–22]) between the particles to cause them to coalesce into a floating raft. For the deionized water experiments, the small and large particles have densities 1025 and 1080 kgm^{-3} respectively. For the experiments on the glycerol-water fluid, both small and large particles have density 1130 kgm^{-3} . The rafts have initial packing fraction of $73 \pm 1\%$.

The raft is enclosed by four boundaries. The initial lengths parallel, L_{x0} , and perpendicular, L_{y0} , to the direction of pulling are $L_{x0} \approx L_{y0} \approx 53 \text{ mm}$. Two hydrophilic acrylic sidewalls are placed along the direction of pulling to keep the particle rafts from touching those walls as the raft is pulled. This reduces the friction while keeping the raft confined.

Two polypropylene plates with sharp edges are used to pull the raft apart. They are held with their bottom surfaces just below the air-liquid interface. As the menisci are pinned at the pullers’ edges, the boundaries can be made either hydrophilic or hydrophobic by adjusting the water level slightly. As shown in the right of Fig. 1(a), for a hydrophilic (hydrophobic) surface, the meniscus points upward (downward) and creates a repulsive (attractive) interaction between the particles and the pulling boundary. When the boundary is repulsive (hydrophilic), it does not contact the raft directly; the expansion of the liquid surface, on which the particles float, creates an affine expansion of the underlying metric along the direction of the pulling velocity. This causes the raft to expand in that direction. When the pullers are attractive, in addition to the expansion of the liquid surface there is also the pulling of the raft by the moving walls to which the raft is connected. In Appendix A, we describe our measurement of the expanding liquid surface; the surface on which the particles sit expands uniformly over time in the pulling direction. We have studied both repulsive and attractive of boundary conditions for the

pullers. They produce similar behavior. The data presented here will be for repulsive conditions.

The two pullers are moved in opposite directions as shown in Fig. 1(a). Each one is moved at a constant speed $V/2$. This allows the center of the raft to remain fixed in the laboratory frame of reference. We vary V in different experiments over several decades: from 2.5 mm/s to 200 mm/s for deionized water and from 0.87 mm/s to 42 mm/s for the glycerol-water mixture. We do not go faster than 200 mm/s with water because we observe significant surface waves, created by pulling at high velocity, that affect our measurements. For glycerol-water experiments, we go to the slowest possible speed that our motor can reliably control. Since $L_x = L_{x0} + Vt$, the liquid strain rate $\dot{\varepsilon} = V/L_x$ across the system decreases monotonically with time. The initial strain rate, $\dot{\varepsilon}_0 = V/L_{x0}$, was varied from $1.6 \times 10^{-4} \text{ s}^{-1}$ to 3.7 s^{-1} . The experiments stop at a maximum liquid strain value $\varepsilon_{max} \sim 1.8$.

III. EXPERIMENTAL RESULTS

As the pulling boundaries are separated, there is a change in the morphology of the raft as micro-cracks, or rifts, begin to form as shown in Fig. 1(b). The images in each column are taken from a single movie of an experiment at fixed velocity at equally spaced values of the liquid strain, ε . The two columns correspond to different pulling speeds.

As the raft expands in the horizontal direction, the rifts become larger, as can be seen in subsequent images in each column. These small cracks, or rifts, are distributed diffusely throughout the entire system. Despite their diverse shapes, the micro-cracks are generally oriented in the direction perpendicular to the pulling direction. The sizes and the horizontal distance between adjacent rifts, which we call the cluster length ℓ , are both fairly uniform in each image.

The morphology depends strongly on the pulling velocity, V , as seen in the difference between the left and right columns of Fig. 1(b). The number of micro-cracks, N_c , and ℓ , both depend strongly on V . When V is small enough, the raft is only slightly sheared although the underlying liquid has been stretched by a factor of 2.5 (*i.e.*, which corresponds to $\varepsilon = 1.5$). After the initial disturbance, the raft remains unchanged for the rest of the expansion; no significant micro-cracks can be observed and the cluster width ℓ remains close to the initial system size, L_{x0} .

With increasing V , the number of rifts, N_c , increases while the cluster size, ℓ , decreases. When V is increased further, the raft stretches along the pulling direction but remains essentially unchanged in the transverse direction except for the edges, which are disturbed by the secondary flow for less viscous fluid such as deionized water. That is, it behaves like a sheet with zero Poisson’s ratio. In the meantime, ℓ decreases almost to the size of a sin-

gle particle, as shown in the right column of Fig. 1(b). Figure 1(c) shows how the internal features change with increasing V : a relatively closely-packed structure gradually turns into clusters with only a few, or sometimes only one, particles in width.

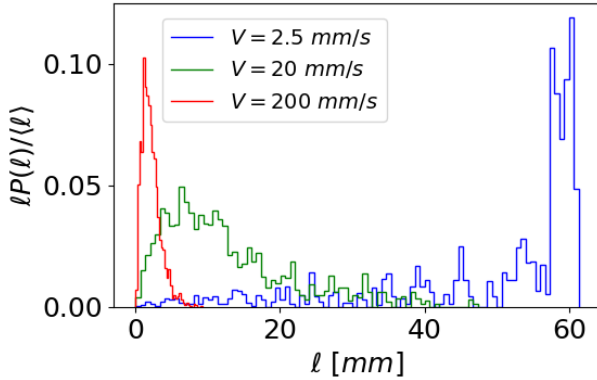


FIG. 2. Distribution of cluster lengths, ℓ , for different velocities at fixed strain in air-water experiments. The probability of cluster length ℓ multiplied by ℓ normalized by $\langle \ell \rangle = \sum \ell P(\ell)$ is plotted versus ℓ at a fixed strain $\varepsilon = 1.0$ with three pulling speeds, V : 2.5 mm/s (blue), 20 mm/s (green) and 200 mm/s (red).

To quantify this observation, we measure the cluster lengths, ℓ , of the raft. The image processing protocols are described in Appendix B. Figure 2 shows the distribution of cluster sizes at a liquid strain $\varepsilon = 1.0$ for different pulling velocities. The results are largely independent of the liquid strain ε for $\varepsilon \gtrsim 0.5$. This indicates that once a rift is formed, it does not collapse at later times. The ordinate is $\ell P(\ell)/\langle \ell \rangle$ where, for each velocity, $P(\ell)$ is the probability of finding a cluster of length ℓ and the average cluster length $\langle \ell \rangle = \sum \ell P(\ell)$. At small V , a large portion of the distribution sits close to the initial cluster size, L_{x0} . (The clusters can be larger than the L_{x0} because the raft can still be slightly stretched at small V .) The distribution shifts to smaller ℓ as V increases. At our highest pulling speed, V , most clusters have lengths between d and $2d$.

Figure 3 shows the average cluster length $\langle \ell \rangle$ versus pulling speed V at a fixed value of the strain, $\varepsilon = 1.0$ for all water and glycerol-water experiments. One can see that $\langle \ell \rangle$ decreases monotonically with increasing V and saturates at high velocities. Because the length of a cluster cannot be significantly larger than the size of the system, L_{x0} , or smaller than a particle diameter, d , we interpolate between the two extremes in our air-water data using:

$$\langle \ell \rangle = \frac{1}{aV^b + 1/(L_{x0} - d_{max})} + d_{max}. \quad (1)$$

This fit is shown in Fig. 3 (a). Fitting to this form gives $b = 1.1 \pm 0.2$ and $a = (1.2 \pm 0.4) \times 10^4$ in SI units.

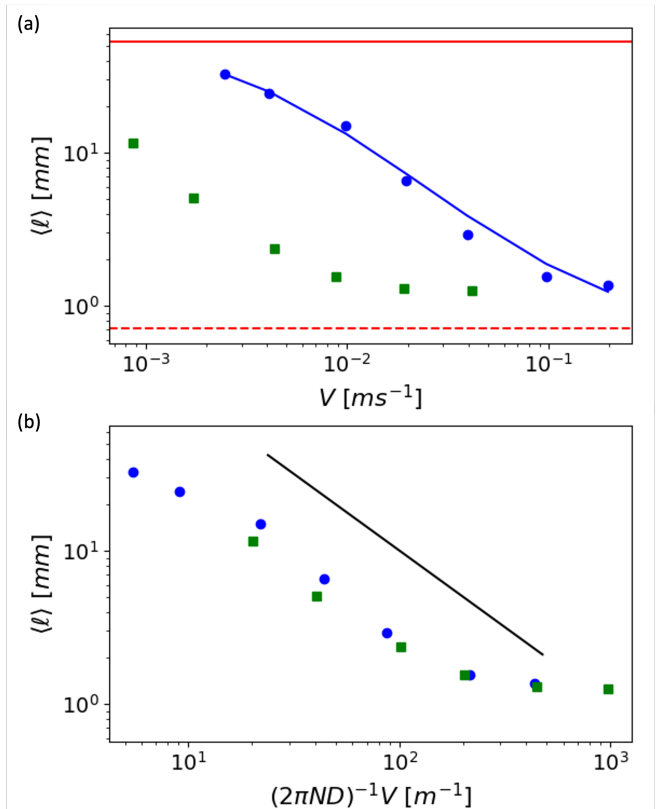


FIG. 3. Averaged cluster length, $\langle \ell \rangle = \sum \ell P(\ell)$, versus pulling speed, V at fixed strain $\varepsilon = 1.0$. (a) The blue and green points are measurements of $\langle \ell \rangle$ versus V for deionized water and glycerol-water mixtures respectively. The blue curve is a fit of Eq. 1 to the water data set. The red solid and dashed lines indicate the initial system size L_{x0} and largest particle diameter d_{max} respectively. (b) The pulling speeds, V , are scaled with $(2\pi ND_w)^{-1}$ and $(2\pi ND_{gw})^{-1}$ derived from Eq. 7. The experimentally measured values of D_w and D_{gw} , the ratio between the lateral capillary force to the Stokes' drag, for the two fluids were used. The black line shows the theoretical prediction for water.

IV. ANALYSIS AND DISCUSSION

To understand the velocity-dependence of the failure morphology, we start with a one-dimensional chain to model our quasi-one-dimensional system. We assume that the Reynolds number, $Re = \rho v \eta / \eta \ll 1$ (where v is the velocity of a particle, η is the dynamic viscosity of the liquid bath, ρ is the density of the liquid) so that the dynamics is overdamped.

At $t = 0$, N identical particles with diameter d are in contact with their neighbors. We assume that one end of the chain is fixed and the other end is pulled at a constant pulling speed V . The positions of the particles along the chain will remain evenly spaced and increase linearly in time due to the affine motion of the fluid. The coordinate of the i^{th} particle is x_i and the distance between the centers of adjacent particles is Δx . The spacing between

the particles increases as $\frac{d\Delta x}{dt} = V/(N-1) \approx V/N$.

We perturb the particles from their equilibrium positions by a small displacement, $u(x)$. Each particle will feel the lateral capillary forces from its two neighbors and the Stokes' drag of the fluid. We use the lateral capillary force calculated in Ref. [21] to obtain an equation of motion. This analysis, although it appears to have the same simple form as a chain of balls connected by linear (or non-linear) springs, is different in three crucial regards: (i) as we shall see, due to the nature of the interparticle potential, the chain is inherently unstable to any expansion, (ii) this leads to relaxation velocity that depends on cluster size which then competes with the expansion velocity and (iii) the particle motions are overdamped.

$$3\pi\eta d\alpha \frac{du(x_i)}{dt} = \pi\sigma dB_o^{5/2}\Sigma^2 \left(-K_1\left(\frac{\Delta x_{i,l}}{L_c}\right) + K_1\left(\frac{\Delta x_{i,r}}{L_c}\right) \right) \quad (2)$$

where $\Delta x_{i,l} = \Delta x + u(x_i) - u(x_{i-1})$ and $\Delta x_{i,r} = \Delta x + u(x_{i+1}) - u(x_i)$. η and σ are the dynamic viscosity and surface tension of the liquid respectively. α is the scaling factor for a submersed sphere and Σ^2 is the dimensionless resultant weight of the particles, determined in Eq. 9 in Ref. [21]. $L_c = \sqrt{\sigma/\rho g}$ is the capillary length, which defines the length scale of the interfacial deflection and the Bond number $B_o = d^2/(4L_c^2) = \rho g d^2/(4\sigma)$ compares the relative importance of gravity and surface tension. At early times, the displacement between particles is small so that we can use the asymptotic form of the modified Bessel's function: $K_1(x) \approx 1/x$ when $x \ll 1$. After using this approximation in Eq. 2, we Taylor expand to first order in $u(x)$ and take the continuum limit. We obtain:

$$\frac{\partial u}{\partial t} = -\left(\frac{\sigma B_o^{5/2}\Sigma^2 L_c}{3\eta\alpha}\right) \frac{\partial^2 u}{\partial x^2} = -D \frac{\partial^2 u}{\partial x^2} \quad (3)$$

Because all the terms inside the parentheses are positive, D is also positive so that this expression has the form of a diffusion equation with a negative diffusion coefficient.

This implies that this system is unstable at all wavelengths; given a chance it will revert back to its un-stretched initial condition. However, to do so involves a competition between the k -dependent relaxation and the pulling velocity, V , which affinely stretches the raft.

We can evaluate this competition by plugging in $u \propto e^{t/\tau} e^{ikx}$ to obtain a characteristic time scale $\tau \propto k^{-2}$. We then extract a characteristic relaxation, or “healing”, velocity by rewriting the solution as $e^{i(kx - \tilde{v}t)} = e^{ik(x - \tilde{v}t)}$ to obtain $v_{heal} = |\tilde{v}| \approx \frac{1}{k\tau}$. This healing velocity depends on the wavelength of the cluster. Larger clusters naturally relax at a slower rate as, in one part of the cluster, the particles come together at the expense of the rest of the cluster where the particles move apart. By comparing the healing velocity, v_{heal} , with the velocity difference between adjacent particles due to the expanding metric of the pulling, V/N , we determine on what (small) scale the system looks relaxed and on what (larger) scale it looks as if it is still being pulled apart. By equating $v_{heal} \approx V/N$, we find the dependence on V of the

crossover or cluster-size wavevector k_{cl} between these two regimes:

$$k_{cl} \approx \frac{3\eta\alpha}{\sigma B_o^{5/2}\Sigma^2 L_c} \frac{V}{N}. \quad (4)$$

or, using $\langle \ell \rangle = 2\pi/k_{cl}$,

$$\langle \ell \rangle \approx 2\pi \frac{\sigma B_o^{5/2}\Sigma^2 L_c N}{3\eta\alpha} V^{-1} \quad (5)$$

$$= \frac{\pi}{48} \frac{\Sigma^2}{\alpha} \frac{d^5(\rho g)^2 N}{\sigma\eta} V^{-1} \quad (6)$$

$$= (2\pi N D) V^{-1}. \quad (7)$$

In the second equation, we have expressed the result in terms of the experimental variables of the liquid and particle parameters. In the last equation, we express the result in terms of a single parameter, D , which is an experimentally measurable quantity as discussed below.

We first compare this result from the model, $\langle \ell \rangle = \frac{1}{a_{th} V^{b_{th}}}$, with the air-water data. The value of the exponent, $b_{th} = 1$, is consistent with the experimental value: $b = 1.1 \pm 0.2$. We also compare the magnitude of the prefactor in the model with that found in the experiment. We use an average value $d = 600 \mu\text{m}$ and the value, $\Sigma^2/\alpha = 0.673$, determined in Ref. [21] for that value of d . We obtain $a_{th} \approx 2.4 \times 10^3 \text{ sm}^{-2}$. When compared with the fitted value $a = (1.2 \pm 0.4) \times 10^4 \text{ sm}^{-2}$, the prefactor of the model only differs from the fitted value by roughly a factor of 5. This is a surprisingly good agreement given that the model neglects all two-dimensional effects that are inherent in the experiment.

In Eq. 3, D is the ratio of the lateral capillary force to the Stokes' drag, a quantity that can be directly measured in experiment. To obtain D , we track the trajectories of two particles at the air-liquid interface as they approach each other as described in Ref. [21, 22]. We evaluate the effect of polydispersity by pairing large and large, large and small, and small and small particles. We weighted-average the measurements of D under the assumption that large-and-small pairs are twice as likely to be found than large-and-large or small-and-small pairs in a well-mixed packing with equal numbers of large and small spheres. The results for both water and glycerol-water mixture are $D_w = (8.0 \pm 4.7) \times 10^{-7} \text{ m}^2\text{s}^{-1}$ and $D_{gw} = (7.8 \pm 4.1) \times 10^{-8} \text{ m}^2\text{s}^{-1}$. These values are very close to the theoretical calculation for a pair of identical spheres with $d = 600 \mu\text{m}$: $D = 7.60 \times 10^{-7} \text{ m}^2\text{s}^{-1}$ and $D = 9.46 \times 10^{-8} \text{ m}^2\text{s}^{-1}$ respectively. Thus the theoretical prediction is consistent with our measurements.

The predicted crossover cluster length, $\langle \ell \rangle$, depends not only on velocity but also on fluid parameters, η , σ and ρ , which are explicit in the negative diffusion coefficient, D , and the size of the system, $N = \frac{L_{x0}}{\langle d \rangle}$. By changing the fluid, we can check the dependence of $\langle \ell \rangle$ on these parameters.

Using our experimental measurements of the diffusion constant, D , for the two liquids, we scale V with $(2\pi ND_w)^{-1}$ and $(2\pi ND_{gw})^{-1}$ and find a good collapse between the water and glycerol-water mixtures, as shown in Fig. 3(b). In this data collapse, the dynamic viscosity contributes the most to the change in D .

V. CONCLUSION

In conclusion, we have observed a velocity-dependent failure morphology in particle rafts floating on an air-liquid interface that is stretched uniformly in one direction. As V increases, the average cluster length of contiguous particles, $\langle \ell \rangle$, decreases monotonically until it reaches the single-particle cut-off. This behavior can be described by a one-dimensional chain model with over-damped dynamics that produces a diffusion equation with a negative diffusion coefficient. We compare the healing velocity, that is the speed at which the particles relax, with the velocity difference between particles produced by the motion of the underlying fluid. The competition between these two velocities gives rise to a crossover length, which separates the scale at which particles coalesce into a cluster from the scale at which the particles become pulled apart.

There remains many interesting features in the system to be understood. One topic which we would like to investigate is how the overall dimensions of the system, L_{x0} and L_{y0} , interact with the micro-crack formation. By concentrating on these rafts, where the microscopic rearrangements as well as the overall fracture dynamics can be assessed, the interaction with the edges can be addressed carefully. Thus, the dynamics and the dependence on system size and aspect ratio might be related to classical fracture mechanics. We also note that this phenomenon of micro-crack formation in rafts is reminiscent of other aspects of failure in the context of material processing. For example, the global shape of the rafts exhibit a change in Poisson's ratio as a function of the pulling speed. At high V , the raft shows a near-zero Poisson's ratio during the stretching. This occurs while most of the raft is still connected as a network and there are evenly distributed micro-cracks throughout the interior. Such behavior is reminiscent of the formation of microstructure in some porous media, such as the expanded polytetrafluoroethylene (ePTFE) [23, 24], which is not well understood.

Although the raft is pulled along one direction, the clusters that are formed do not show a systematic orientation with respect to the flow. One might have expected that not only the rifts, but the clusters themselves, would show some aspect of the symmetry of the dynamics. This is not the case and suggests that there are an important aspects of cluster formation that remain to be examined. In particular, it is of our interest to explore the failure morphology of a raft pulled uniformly in a radial flow. In radial expansion, there is no single tensile axis in the

system. Such an expanding two-dimensional metric, as distinct from the one-dimensional pulling we have used here, might give us further insight into the situation of distributed failure in a fully three-dimensional system. Such an experiment is more relevant to the situation of cosmological expansion.

VI. ACKNOWLEDGEMENT

We thank Michelle Driscoll who made some of the first movies of these expanding rafts in our lab. We are also grateful to Daniel Hexner, James Sethna, Vincenzo Vitelli, Sungyon Lee and Xiang Cheng for enlightening discussions about how to think about this system. This work was supported primarily by the National Science Foundation (MRSEC program NSF-DMR 2011854). KIT was supported in part by Government Scholarship to Study Abroad by the Ministry of Education in Taiwan and by the Simons Foundation for the collaboration Cracking the Glass Problem Award #348125.

Appendix A: Particle Image Velocimetry

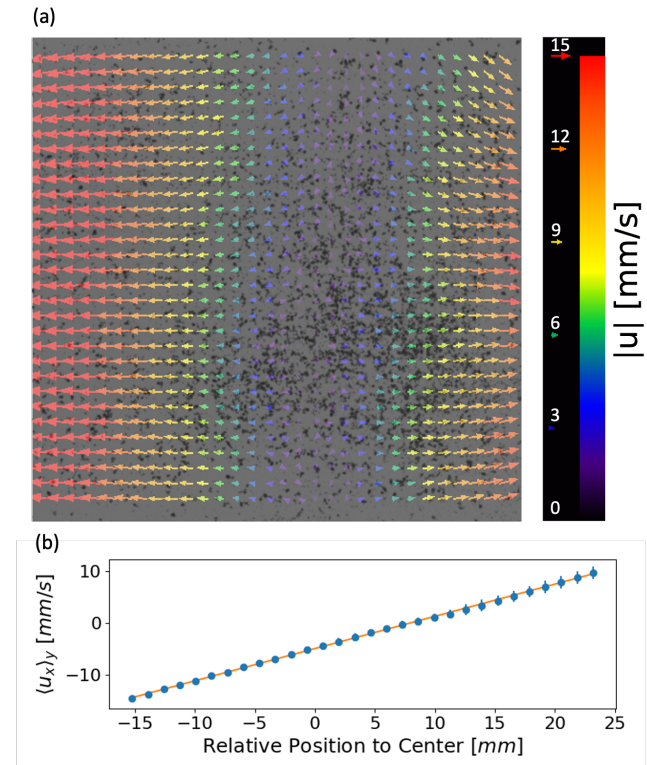


FIG. 4. The Particle Image Velocimetry result of the two pullers moving at 2.5 mm/s in the opposite directions on water. (a) The color bar shows the magnitude of the velocity. (b) The average velocity parallel to the pulling direction increases linearly with respect to their horizontal positions.

To measure the expansion of the liquid surface due to the extension of the pullers, we perform Particle Image Velocimetry (PIV) measurement on water at $V = 2.5 \text{ mm/s}$. The result is shown in Fig. 4. We spread a dilute layer of very light, non-interacting floating particles on the water surface prior to pulling. By tracking the motion of these particles and computing the correlation between adjacent frames, we determine that the underlying fluid flows lead to an affine expansion of the surface; the spacing of the particles in the direction of the pulling increases linearly in time. The PIV map of nearly the entire surface is shown in Fig. 4(a). The particle velocities are independent of the direction perpendicular to the pulling. Fig. 4(b) shows the gradient of the velocity is constant in the direction of pulling.

Appendix B: Image Recording and Processing

The motions of the particles are recorded using Phantom VEO 640S and Prosilica GX3300 cameras. The frame rates are adjusted so that the displacement of a particle between frames is no larger than d_{max} . In our experiments, we are interested in measuring the size of the clusters between adjacent rifts in a raft. To obtain this information, we do not want to include the microscopic holes between the spherical particles that would be there even when the raft is closely packed.

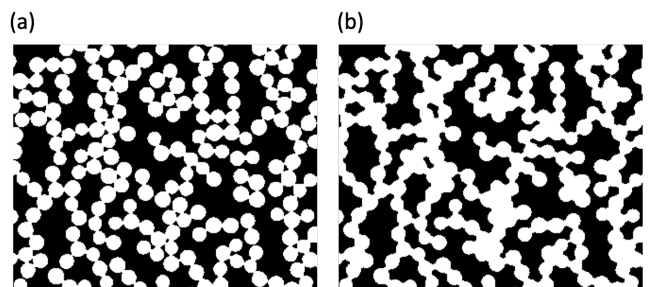


FIG. 5. Example of procedure to remove the spacings between particles that touch each other even in a compact raft. (a) The original image of the raft is binarized so that the particles are white and the background is black. (b) The radius of each particle in (a) is increased so that the small gaps between particles, due to the fact that spheres cannot tile space fully, are no longer present. The perimeter of the new clusters are then decreased by the same amount as they were originally expanded. This closes the gaps internal to the raft but leaves only the gaps or rifts that are formed due to raft expansion.

After thresholding the images to separate the particles from the background, we dilate each of the particles by a fixed amount so that these small holes disappear. This morphological operation to the binarized images results in an increase in the area of the particles. The size of the dilation kernel is determined by the square root of the average hole area in the initial packing. A reverse morphological operation (erosion) is then performed to shrink the clusters around their perimeters while leaving the particles swelled on the interior. This procedure removes the holes between particles that are comparable to the spacing in the original packings so that only the small newly-created cracks, the rifts due to the raft expansion, remain. This is shown in Fig. 5. To measure the cluster lengths in the horizontal direction, we take one-pixel height horizontal slices of the processed images.

[1] J. Fineberg and M. Marder, Instability in dynamic fracture, *Physics Reports* **313**, 1 (1999).

[2] J. L. González-Velázquez, *A Practical Approach to Fracture Mechanics*. (Elsevier, San Diego, 2021) p. 286, description based upon print version of record.

[3] L. B. Freund, *Dynamic fracture mechanics*, Cambridge monographs on mechanics and applied mathematics (Cambridge University Press, Cambridge ; New York, 1990) p. 563.

[4] A. T. Zehnder, *Fracture mechanics*, Lecture notes in applied and computational mechanics ; (Springer, Dordrecht ; New York, 2012) p. 223.

[5] J. Chakrabarty, *Theory of plasticity*, 3rd ed. (Elsevier/Butterworth-Heinemann, Amsterdam ; Boston ; Oxford, 2006) p. 882.

[6] Z. P. Bažant and J. Planas, *Fracture and size effect in concrete and other quasibrittle materials* (Routledge, 2019).

[7] M. L. Falk and J. Langer, Deformation and failure of amorphous, solidlike materials, *Annual Review of Condensed Matter Physics* **2**, 353 (2011), <https://doi.org/10.1146/annurev-conmatphys-062910-140452>.

[8] A. Nicolas, E. E. Ferrero, K. Martens, and J.-L. Barrat, Deformation and flow of amorphous solids: Insights from elastoplastic models, *Rev. Mod. Phys.* **90**, 045006 (2018).

[9] S. Roux, A. Hansen, H. Herrmann, and E. Guyon, Rupture of heterogeneous media in the limit of infinite disorder, *Journal of Statistical Physics* **52**, 237 (1988).

[10] I. Malakhovsky and M. A. J. Michels, Effect of disorder strength on the fracture pattern in heterogeneous networks, *Phys. Rev. B* **76**, 144201 (2007).

[11] M. J. Alava, P. K. V. V. Nukala, and S. Zapperi, Role of disorder in the size scaling of material strength, *Phys. Rev. Lett.* **100**, 055502 (2008).

[12] A. Shekhawat, S. Zapperi, and J. P. Sethna, From damage percolation to crack nucleation through finite size criticality, *Phys. Rev. Lett.* **110**, 185505 (2013).

- [13] M. M. Driscoll, B. G.-g. Chen, T. H. Beuman, S. Ulrich, S. R. Nagel, and V. Vitelli, The role of rigidity in controlling material failure, *Proceedings of the National Academy of Sciences* **113**, 10813 (2016), <https://www.pnas.org/content/113/39/10813.full.pdf>.
- [14] H. Xiao, R. J. S. Ivancic, and D. J. Durian, Strain localization and failure of disordered particle rafts with tunable ductility during tensile deformation, *Soft Matter* **16**, 8226 (2020).
- [15] M. Arciniaga, C.-C. Kuo, and M. Dennin, Size dependent brittle to ductile transition in bubble rafts, *Colloids and Surfaces A: Physicochemical and Engineering Aspects* **382**, 36 (2011), a collection of papers from the 8th EUFOAM Conference and the Meetings of COST Actions D43 and P21.
- [16] Y. Wang, P. Kanjanaboops, S. P. McBride, E. Barry, X.-M. Lin, and H. M. Jaeger, Mechanical properties of self-assembled nanoparticle membranes: stretching and bending, *Faraday Discuss.* **181**, 325 (2015).
- [17] N. Lu, Z. Suo, and J. J. Vlassak, The effect of film thickness on the failure strain of polymer-supported metal films, *Acta Materialia* **58**, 1679 (2010).
- [18] A. Skjeltorp and P. Meakin, Fracture in microsphere monolayers studied by experiment and computer simulation, *Nature* **335**, 424 (1988).
- [19] A. F. Routh, Drying of thin colloidal films, *Reports on Progress in Physics* **76**, 046603 (2013).
- [20] V. Paunov, P. Kralchevsky, N. Denkov, and K. Nagayama, Lateral capillary forces between floating submillimeter particles, *Journal of colloid and interface science* **157**, 100 (1993).
- [21] D. Vella and L. Mahadevan, The “cheerios effect”, *American journal of physics* **73**, 817 (2005).
- [22] M.-J. Dalbe, D. Cosic, M. Berhanu, and A. Kudrolli, Aggregation of frictional particles due to capillary attraction, *Phys. Rev. E* **83**, 051403 (2011).
- [23] R. W. Gore, Process for producing porous products (1976), uS Patent 3,953,566.
- [24] T. Kitamura, K.-I. Kurumada, M. Tanigaki, M. Ohshima, and S.-I. Kanazawa, Formation mechanism of porous structure in polytetrafluoroethylene (ptfe) porous membrane through mechanical operations, *Polymer Engineering & Science* **39**, 2256 (1999).